Electrochemistry Communications 187 (2026) 108161

Contents lists available at ScienceDirect

Electrochemistry Communications

journal homepage: www.elsevier.com/locate/elecom

Towards greener MCFCs matrix: a new solvent for tape casting fabrication

Lucia Cardona [a], Riccardo Risso [a], Juan Pedro Pérez Trujillo [b], Dario Bove [a,*], Carina Lagergren [b], Maurizio Archetti [c], Barbara Bosio [a]

[a] Department of Civil, Chemical and Environmental Engineering, University of Genova, Via Opera Pia 15, 16145 Genova, Italy
[b] Applied Electrochemistry, Department of Chemical Engineering, KTH Royal Institute of Technology, SE-100 44 Stockholm, Sweden
[c] Ecospray Technologies S.R.L., 15050 Alzano Scrivia, Italy

ARTICLE INFO

Keywords:
High-temperature fuel cells
Molten carbonate fuel cells
Ceramic matrix
Alternative fuel cell components
Fuel cell production processes
Energy transition

ABSTRACT

Carbon capture and storage plays a fundamental role in achieving the ambitious goal of the 2030 Agenda to eliminate carbon dioxide emissions by 2050. One of the most promising technologies for this purpose is the Molten Carbonate Fuel Cell (MCFC), a device capable of producing energy while capturing carbon dioxide from industrial flue gases.

In this technology, a key component is the ceramic matrix that is filled with molten carbonates. This work aims to optimize both its performance and the production process, with a focus on making it more environmentally friendly by eliminating toluene, a component commonly used in literature for its production. The developed matrix formulation was characterized using mercury porosimeter and scanning electron microscopy (SEM), revealing uniform morphology across the entire surface, with porosity and pore size distribution values consistent with those reported in the literature.

Once the optimal physical properties were achieved, the electrochemical performance of the matrix was assessed through a comprehensive testing procedure using reference electrodes. Additional tests were carried out by varying the cathode gas composition and operating temperature, as well as replicating real industrial exhaust conditions that require effective CO_2 reduction solutions.

In all test scenarios, the matrix exhibited performance values fully in line with literature benchmarks, confirming its potential and marking a significant improvement in the manufacturing process.

Overall, this study provides a comprehensive link between manufacturing parameters, material properties, and electrochemical performance, contributing to the optimization of MCFC matrices for carbon capture applications.

1. Introduction

In recent years, carbon capture and energy transition have emerged as some of the greatest challenges to address. Numerous climate actions developed under the framework of the Sustainable Development Goals (SDGs) aim to achieve these critical objectives. One of the most pressing issues is the emission of carbon dioxide, which is directly linked to climate change and the global rise in temperatures. To tackle this challenge, a phased approach has been adopted. The first milestone is set for 2030, with the goal of reducing emissions by 55% compared to 1991 levels [1].

Carbon Capture and Utilization (CCU) covers a wide range of applications in which carbon dioxide is captured and subsequently used either directly or indirectly. The initial stage of this process, carbon capture, can be achieved through different technologies, depending on the specific application. The most common approaches include post-combustion carbon capture, which involves physical or chemical adsorption/absorption techniques, membrane separation, and chemical reactions. A key factor uniting these technologies is the high energy demand required for their operation. A possible solution to resolve this issue is the Molten Carbonate Fuel Cell (MCFC), which is a well-established technology for energy production. This technology has been evolving as a novel approach, particularly noteworthy for its dual capability: it not only generates energy but also effectively captures and segregates carbon dioxide, making it a significant tool in the pursuit of sustainable energy solutions [2,3].

This system, owing to its modularity, can have its power adjusted across various ranges (from kW to MW, [4]), making it highly adaptable for application in numerous sectors. The basic cell is comprised of six main components: two electrodes that catalyze the electrochemical

* Corresponding author.
E-mail address: dario.bove@unige.it (D. Bove).

https://doi.org/10.1016/j.elecom.2026.108161
Received 6 October 2025; Received in revised form 29 March 2026; Accepted 30 March 2026
Available online 1 April 2026

reaction; an electrolyte, which in this application is based on molten carbonate and guarantees the flow of charge carriers through the internal cell circuit; a matrix that serves as the electrolyte's support structure; and two current collectors, which enables both gas distribution and the transfer of electrons. The following Fig. 1 illustrates the mechanism behind the functioning of the cell. Carbonate ions migrate from the cathode side to the anode side through the matrix sheet, which is impregnated with the electrolyte. To enable reactions (1) and (2), the circuit has to be closed externally, connecting the two electrodes to enable the electron migration to happen.

$$H_2 + CO_3^{2-} \rightarrow H_2O + CO_2 + 2e^- \quad (1)$$

$$CO_2 + 2e^- + {}^1\!/\!_2 O_2 \rightarrow CO_3^{2-} \quad (2)$$

$$H_2 + {}^1\!/\!_2 O_2 + CO_{2(\text{Cathode})} \rightarrow H_2O + CO_{2(\text{Anode})} \quad (3)$$

Each component possesses distinct characteristics that must be optimized to ensure high cell performance in terms of both power output and electrical resistance, [5]. The matrix is a key component in MCFCs, as it plays a crucial role in separating the anode and cathode compartments while retaining the electrolyte. Because of its importance, the matrix has been investigated not only as an inert structural component, as in this study, but also as an active layer capable of exhibiting ionic conductivity. In particular, some works have explored the use of ceramic materials typically employed as electrolytes in Solid Oxide Cells, thus enabling dual anion conductivity (CO_3^{2-} from the MCFC electrolyte and O^{2-} from the SOFC electrolyte), which can lead to increased power density [6,7].

The purpose of this study is the optimization of the inert matrix, the most critical component of the cell through chemical and physical analysis and characterization followed by in-cell testing. The main novelty of this work lies in the innovative matrix fabrication method, which replaces the toxic solvent, toluene, commonly used in literature with an eco-friendly alternative. The properties of this solvent, referred to as S1, were provided by Ecospray Technology under a commercial agreement. For confidentiality reasons, the commercial name cannot be disclosed; however, to ensure reproducibility, the following experimental average characteristics are reported in Table 1 with a comparison with Toluene.

Based on well-established principles of ceramic slurry processing, solvent properties strongly influence slurry rheology, particle dispersion, and drying kinetics. In particular, lower solvent viscosity, 0.50 mPa·s for S1 compared to 0.56 mPa·s for toluene, enhances particle mobility and dispersion, thereby reducing agglomeration phenomena and promoting the formation of a more homogeneous green matrix [8].

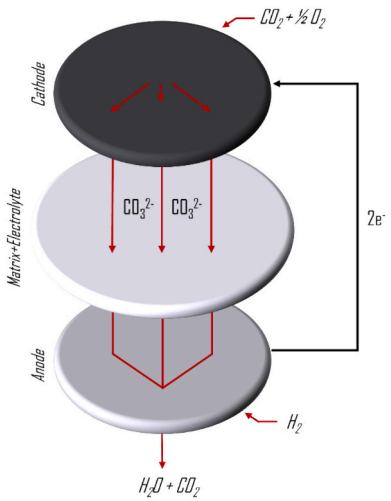

Fig. 1. Schematic of the MCFC working principle.

Table 1
Comparison of the physical properties of toluene and solvent S1,

	Toluene	Solvent S1
Density @20 °C [kg/m^3]	870	790
Molecular weight [g/mol]	92	53
Viscosity @25 °C [mPa·s]	0.56	0.50
Boiling point [°C]	110	65
Surface tension [nN/m]	28.5	23.0
Cost and safety	Higher cost, toxic	Lower cost, non-toxic

Furthermore, solvents with lower molecular weight and density (53 g/mol and 790 kg/m^3 for S1, vs 92 g/mol and 870 kg/m^3 for toluene) are associated with increased molecular mobility and diffusivity, which can facilitate a more uniform solvent removal during the drying stage [9].

Evaporation kinetics are primarily governed by solvent vapor pressure and boiling point, among other processing-dependent factors, with S1 exhibiting a lower boiling point of 65 °C versus 110 °C for toluene. When properly controlled, this favors the development of smaller, more uniform pores while limiting drying-induced defects [10]. However, shifting from a traditional aromatic solvent like toluene to the S1 system requires an optimization of the mechanical mixing energy. According to standard processing guidelines [11], low-viscosity systems often require an increase in rotational speed (typically in the range of ~15–25% higher RPM, depending on mill geometry and media loading) to maintain the grinding media in an optimal cascading motion. This increase in RPM compensates for the lower drag force of the S1 medium, ensuring sufficient shear stress to break down hard agglomerates.

This mechanical adjustment ensures that the lower surface tension of S1, approximately 23.0 mN/m compared to 28.5 mN/m for toluene, is fully exploited to minimize capillary stresses during drying [12]. According to the Young–Laplace equation, this reduction in surface energy lowers the mechanical tension on the pore walls, preventing structural collapse and limiting defects such as warping. Consequently, the S1 system can enable the production of thicker green tapes with higher packing density and improved structural integrity.

Also, the use of this solvent instead of toluene results in an approximate 40% reduction in solvent purchase cost, which may positively impact the overall economics of matrix manufacturing.

Additionally, several tests were carried out by varying the cathode-side gas composition to evaluate its impact on cell performance and to simulate real application scenarios in both maritime and steelmaking environments, which are representative examples of hard-to-abate sectors in terms of CO_2 emissions.

This integrated approach, combining process innovation, material characterization, and functional testing under realistic operating conditions, provides new insights into the relationship between matrix manufacturing parameters and MCFC performance, addressing a key challenge for the advancement of this technology.

2. Experimentation

As mentioned above, the matrix layer plays a fundamental role in retaining the carbonate while ensuring its chemical and physical stability. This stability is critical to maintaining gas segregation between the two compartments: the fuel side and the oxygen side. For these reasons, numerous microstructural characteristics of the matrix must be analyzed to uptake electrolyte and hinder gas diffusion. The literature highlights the most important ones as being, [13]:

- Porosity: 50–70%;
- Surface area: > 10 m^2/g;

- Pore dimensions: < 1 μm;
- Gas crossover: ≈ 0.

The matrix layer is typically fabricated using the tape-casting method, which involves a ceramic slurry based on lithium aluminate, $LiAlO_2$, as the raw powder. According to the literature, several recipes have been developed over the years for this manufacturing process. However, a common challenge associated with these methods is the substitution of a toxic solvent, toluene, to produce the slurry phase. Toluene is an organic solvent known for its harmful effects on human health and the environment [14].

The primary goal of this experimental campaign, conducted at University of Genoa, was to completely replace toluene with other organic solvents in order to achieve improvements in health, safety, environmental, and operational factors, making the production of the matrix one step closer to a potential future scale up to industrial scale. In terms of solvent waste management and recovery costs, the use of toluene presents greater challenges compared to other organic solvents, [15].

In the standard matrix manufacturing process, the sintering step is not included, as this thermal treatment takes place directly during the startup phase of the cell stack. For this reason, the matrix sheet produced through the tape casting, which still contains organic compounds such as binders and plasticizers, is commonly referred to as the "green" matrix. To replicate real operating conditions and assess the matrix's behavior within the cell, the green sheet is brought to high temperature, matching that of actual cell operation, to observe the release of organic compounds and study the resulting material structure.

After the sintering process, based on the *Thermogravimetric Analysis*, TGA, the following analyses were made:

- *Scanning Electronic Microscope, SEM*, performed to evaluate the surface homogeneity and the first determination of pores dimensions;
- *Mercury Intrusion Pore Size Analyzers*, which allows to determine the material porosity, surface area and pore size distribution.

At the end, the matrix was used as an active component in a single MCFC cell, which was subjected to electrochemical testing to assess its performance and contribution to overall cell behavior. This evaluation involved measuring the cell's internal resistance, which is directly influenced by the matrix configuration, as well as the overall power output of the cell. These analyses were conducted at KTH, Royal Institute of Technology in Stockholm. In particular, the analyses performed were:

- Polarization curve, which allows to determine the cell power. Several curves were conducted by varying the gas composition on the cathode side;
- Electrochemical Impedance Spectroscopy, which allows to evaluate the different phenomena that contribute to the overall cell electrical resistance, at standard condition and by varying the cathode composition.

2.1. Shaping

The manufacture of this sheet is based on tape-casting method, which is the standard approach reported in the literature. Among the most recent institutions that have studied and developed this process include Korea Institute of Science and Technology, KIST, and Warsaw University of Technology, WUT, [16,17].

The experimental campaign conducted for this study focused on the substitution of toxic compounds rather than modifying the process itself. Accordingly, the base manufacturing procedure adopted for the production of the ceramic matrices follows established approaches reported in the literature by KIST and WUT [16,17]. Consequently, the procedure employed remains consistent with those used in previous studies and can be summarized as follows: Fig. 2.

Each component results necessary to give the slurry and the green matrix itself specific characteristics, [13]:

- Solvents: these are used to allow for a complete homogenization of all chemical compounds present in the mixture to happen, while also activating the plasticizer and binder mixture;
- Raw powder: the basic matrix component. It is ceramic, commonly Lithium Aluminate, $LiAlO_2$;
- Dispersant: it allows for improvement in the slurry rheology and prevents agglomeration;
- Defoamer: this compound helps to eliminate the air inclusions that occur during the ball milling process and subsequent drying process;
- Binder: used to improve strength;
- Plasticizer: it gives improvement in terms of viscosity and grants matrix flexibility.

The milling step ensures slurry homogeneity, which is essential to prevent defects during casting and cell operation. To achieve this, the rotational speed was optimized to 300 RPM (representing a 20% increase compared to the 250 RPM of the reference WUT formulation [17]), a necessary adjustment to maintain the optimal cascading motion within the lower-viscosity S1 medium. Such enhanced homogenization is critical to prevent cracks during the sintering process and, consequently, within the operational cell, thereby mitigating the risk of gas crossover and ensuring the long-term structural integrity of the electrochemical system.

During the degassing step, performed using a vacuum pump, the primary goal is to eliminate air bubbles introduced during the milling process. This step improves slurry homogeneity, preventing crack formation during drying. Once degassing is complete, the slurry is ready for casting. Tape casting was performed with a blade gap of 3.5 mm on a Mylar support, which served as a flat support for the matrix casting. This height determines the final thickness of the green matrix and, consequently, the porous volume to be filled by the electrolyte, molten carbonate.

The final step is the drying process, which is carried out in air for 24 h. After this, the green matrix is ready for use within the cell or for the previously described analyses.

After the drying process, the matrix appears homogeneous and evenly distributed, with a thickness of *0.3 mm*. In the Fig. 3 the green matrix is shown.

2.2. Characterization analysis

Given the critical role of this layer, its characterization is essential to minimize the risk of failure during the operational lifespan of the cell. SEM and Mercury Intrusion Pore Size analyses were conducted on the sintered matrix. This sintering process was conducted by using, as oven, Carbolite Gero, CWF1200. In order to identify the appropriate sintering step required to completely remove the organic components present in the cell, a Thermogravimetric Analysis (TGA) was carried out, as shown in Fig. 4.

The graph displays two y-axes: one corresponding to the derivative weight percentage and the other to the total weight loss percentage. The first degradation peak, observed at around 250 °C, is attributed to the decomposition of the binder. The second, more pronounced peak at approximately 350 °C, corresponds to the degradation of the plasticizer. The total weight loss was about 35%, which aligns with expectations. Initially, the solid-to-liquid ratio of the slurry was approximately 81%, decreasing during the drying step due to solvent evaporation. Consequently, the remaining organic components (binder and plasticizer) account for about 35% of the total mass, consistent with the weight loss detected in the TGA.

The sintering ramp used, based on the TGA results, is illustrated in Fig. 5. Organic solvents evaporate during the drying process.

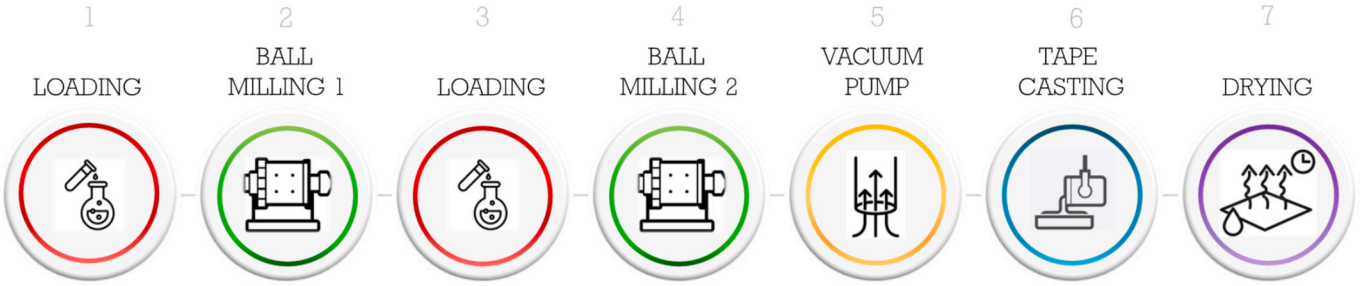

Fig. 2. Matrix manufacturing procedure, based on 7 steps.

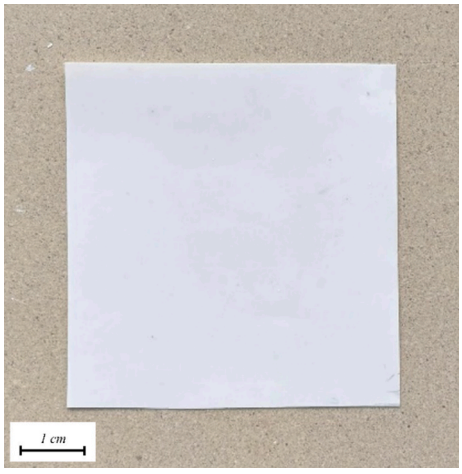

Fig. 3. Green Matrix layer fabricated by the tape casting technique. (For interpretation of the references to colour in this figure legend, the reader is referred to the web version of this article.)

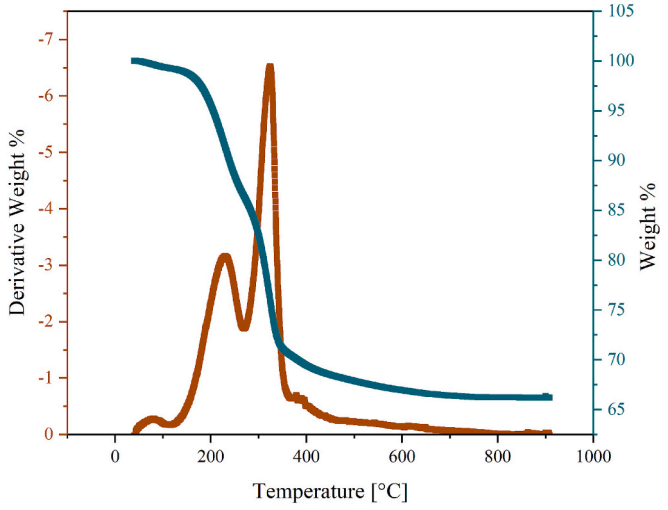

Fig. 4. TGA of the green matrix performed under a N_2 atmosphere, from 25 °C to 900 °C. The figure shows both the weight loss and its derivative as a function of temperature.

Consequently, the primary components, in terms of weight, to be eliminated are only binder and plasticizer, which respectively degrade at 250 °C and 350 °C. To facilitate their degradation, the temperature ramp includes two dwelling steps at these specific temperatures. Finally, the operative temperature, 650 °C, is reached to simulate cell conditions.

SEM technique provides an overview of the sheet surface, with a particular focus on granulometry. The instrument used was ZEISS Sigma

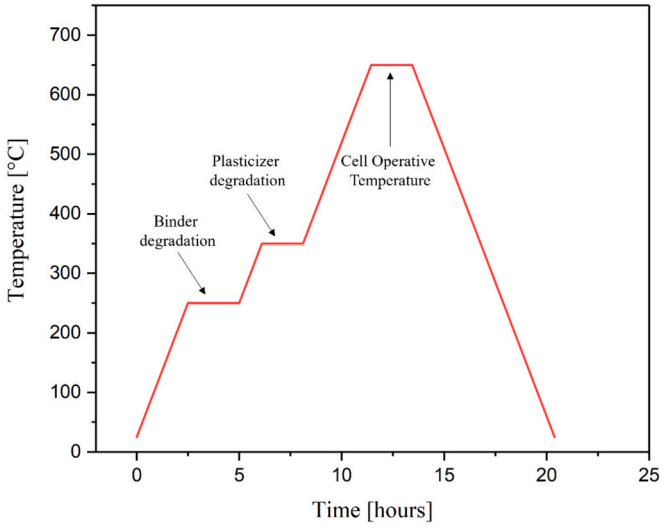

Fig. 5. Sintering Ramp based on the TGA results to degrade all the organic compounds.

360.

This analysis was conducted at several magnitudes, x5000 and x10000, x20000 at 15 kV (Fig. 6). The backscattered electrons provide detailed information on surface morphology.

The ×5000 magnification provides a general view to assess the homogeneity of the matrix, while the ×10,000 and x20000 magnifications offer a closer look to examine the pore dimensions. In the Fig. 6 (A) and (B), morphology appears homogeneous and free of imperfections. At the same time, the Fig. 6 (C) reveals the presence of pores measuring ranging from 1.5 μm down to less than 0.5 μm.

Using Mercury Intrusion Pore Size Analyzer, numerous characteristics were evaluated, including porosity, surface area and pore size distribution. The instrument is PoreMaster GT60 and it consists of two sections, [18]:

- Low pressure section measures the largest pores up to 6 μm using pneumatic pressures until 30 psi;
- High-pressure section operates at 60,000 psi and is capable of measuring pore sizes as small as 3 nm.

Given that, according to the literature, the pore sizes of this layer are below 1 μm, high-pressure analysis was therefore carried out.

The first significant result is the matrix porosity, which represents the percentage of void space within a solid. This result is derived from two distinct contributions, [18]:

- Interparticle porosity, measured during the low-pressure analysis using the following formula:

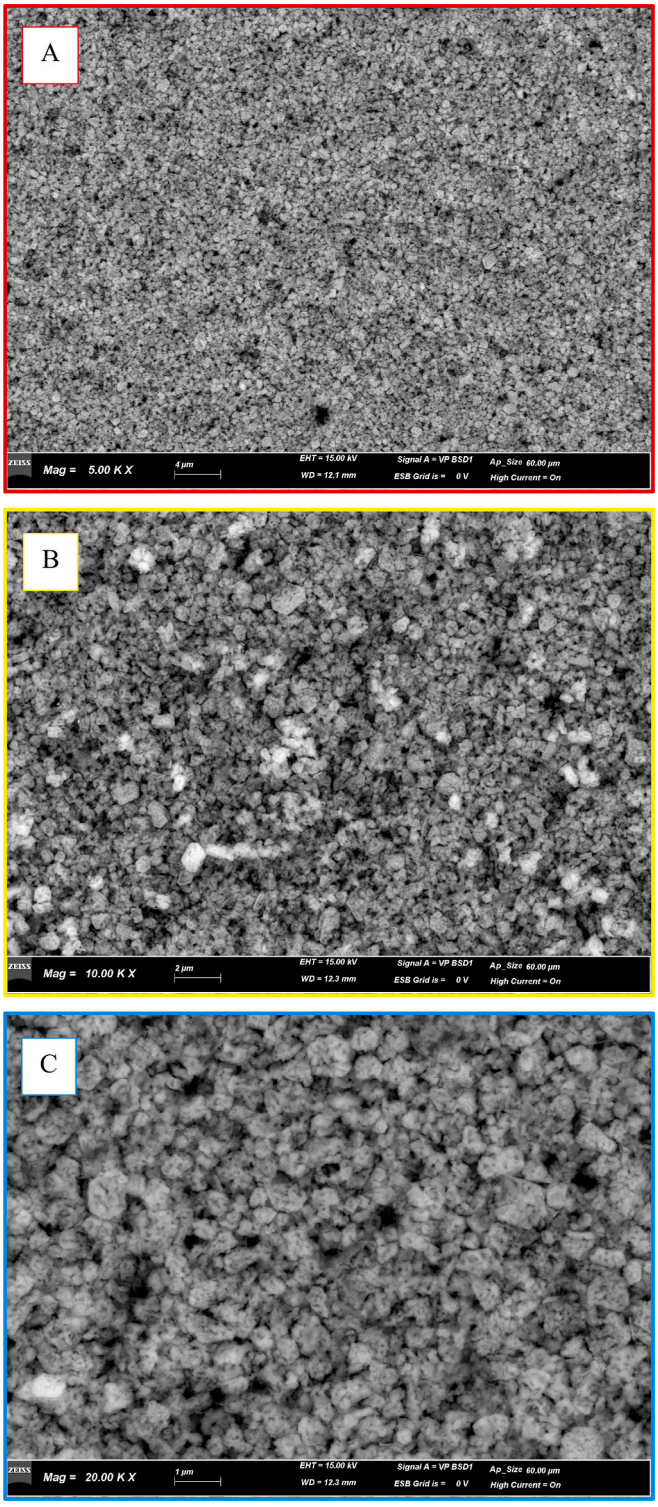

Fig. 6. SEM images, x5000 (A), x10000 (B), x20000 (C) magnifications. The images clearly show the pore size and porosity of the matrix.

$$\text{Interparticle porosity}(\%) = 100\frac{V_v}{V_b} \quad (4)$$

- Intraparticle porosity, measured during the high-pressure analysis using the following formula:

$$\text{Intraparticle porosity}(\%) = 100\frac{V_t - V_v}{V_b} \quad (5)$$

The volumes considered are defined as follows: bulk volume, V_b, volume of mercury intruded up to the interparticle measurement, V_v, and the total volume of mercury intruded up to the maximum pressure, V_t.

The porosity of this matrix is in complete agreement with the literature, it is approximately *62%*, respectively *8%* interparticle, and *54%* intraparticle.

Another useful graph for understanding the matrix's characteristics is the pore volume distribution as a function of pore size. By analyzing this graph, it is possible to observe how the intruded volume varies with changes in the pore size distribution. In Fig. 7, the curve illustrates the variation in pore volume. On the y-axis, this is expressed as the derivative of the volume of mercury able to penetrate the pores, while the x-axis represents the pore size.

At the *50%* mark of the cumulative percentage, the pore diameter corresponds to *0.167* µ*m*. In the following Table 2 there are the main percentages of the pore diameter:

The surface area represents the interstitial surface of the pores per unit mass of the analyzed material. This parameter is crucial for increasing the triple phase boundary, the region where gas, electrolyte, and electrode come into contact and where the electrochemical reaction effectively takes place. A high surface area is essential for facilitating the electrochemical reaction, and moreover for determining the appropriate amount of electrolyte to be added during testing. The measured value is *15.042* m^2/g, it is in line with the values proposed in the literature [13].

2.3. Testing and station set-up

The test station consists of concentric ceramic tubes arranged vertically inside a metallic support, Fig. 8. There are two concentric tubes for each electrode, the smaller tube inside is used to feed the gases to the electrode, while the external one is needed both to allow for the release of the gases but also for the structural stability of the system. Connecting the tubing for the two electrodes is the cell housing, composed of a thick ceramic cylinder. This housing is where the cell itself is located, in layers from bottom to top, starting from the current collector in nickel, followed by the anode. Above the anode, two layers of matrix are positioned, in order to achieve the thickness required to keep the electrolyte and to guarantee the separation of the anode and the cathode side. Although the electrolyte is in powder form, it is pressed into a round-shaped tablet under 10 tons of pressure before being placed above the matrix. The last two components are the cathode and, in the end, a

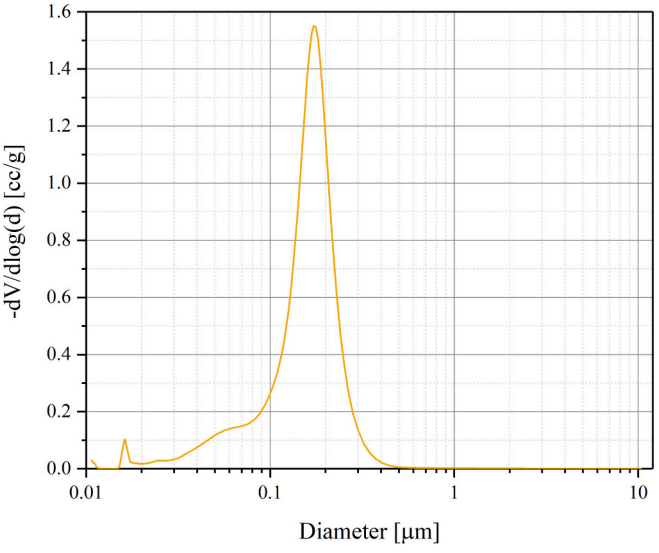

Fig. 7. Pore Volume Variation in function of the Pore Diameter performed using Mercury Intrusion Pore Size Analyzer.

Table 2
Pore size distribution.

D10	*0.222 μm*
D50	*0.167 μm*
D90	*0.069 μm*

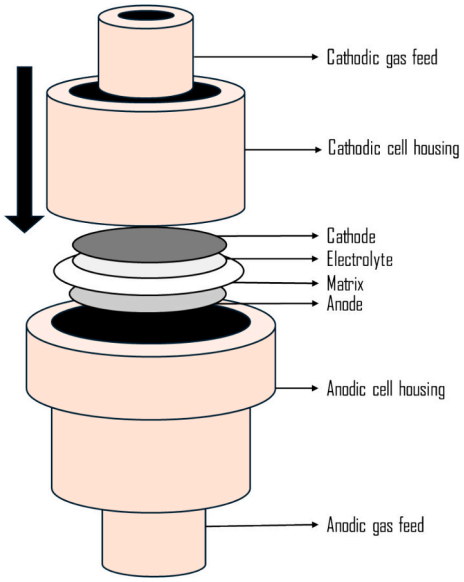

Fig. 8. Cell station setup, showing the gas feed, the cell housing, and the arrangement of the different layers that constitute the cell.

stainless-steel current collector. Then another ceramic tubing is inserted from above, to seal the housing completely. Inside this tubing is a smaller concentric tube, which is positioned in contact with the cathode, and a load will be applied to guarantee good electrical contact with the fuel cell. The cell housing itself is positioned inside a furnace in order to guarantee controlled heating and temperature control during the cell operation.

For both gas lines that feed into the cell a heating tube is applied before entering the cell. This has two reasons, firstly the gas is humidified through heated evaporators the gas is flowed through, and secondly this avoids cooling the cell down too much, as it is true that the cell is producing heat, but the scale is too small for this heat to effectively counteract the various forms of heat dissipation and the temperature.

The test was made utilizing a premixed gas composition to reduce the variables that could affect the test results, the standard compositions of these gases can be seen in Table 3, downstream of the humidifier.

The components used to perform these tests were:

- Two electrodes, an anode and a cathode, made of Ni + 5%$_{wt}$ Al and lithiated NiO, respectively, with a diameter of 19 mm and a thickness of 0.5 mm;

Table 3
Standard gas composition used for anodic and cathodic feed.

	Compounds	Inlet Standard Composition [vol%]
Cathode gas	CO_2	28.8
	O_2	14.4
	H_2O	4.0
	N_2	52.8
Anode Gas	CO_2	16.0
	H_2	64.0
	H_2O	20.0

- Two matrix sheets composed of γ-$LiAlO_2$, with a diameter of 25 mm and a thickness of 0.3 mm;
- Electrolyte powder, a Li_2CO_3/K_2CO_3 eutectic mixture (62/38%$_{mol}$). The amount of powder was calculated according to the work reported by Perez Trujillo et al. [19], also considering the porosity of the layer measured by Mercury Intrusion Pore Size Analyzer. The adequacy of electrolyte filling under the present testing conditions was further supported by the stable resistance evolution over time, indicating effective ionic conduction and no evidence of gas crossover.
- Two current collectors, based on Ni for the anode side and AISI 316 for the cathode side.

3. Results and discussion

Several campaigns were conducted to gain a deeper understanding of both the matrix and cell behavior under various operating conditions:

3.1 Standard condition;
3.2 Temperature variation;
3.3 Cathode gas composition variation;
3.4 Real application conditions.

The polarization curve is a characteristic feature of both the intrinsic properties of the cell materials and the quality of the cell assembly, as it directly reflects the electrochemical performance of the system. This curve illustrates the relationship between the operating current and voltage, providing essential information for evaluating the cell's behavior and allowing the identification of key performance parameters, such as:

- OCV (Open Circuit Voltage);
- Peak power density, which typically represents the optimal working point;
- Limiting current density, indicative of mass transport limitations.

EIS technique measures the impedance of a system over a range of frequencies. In particular, the instrument applies a small sinusoidal perturbance for the input current or voltage (in the current study voltage was used) in order to limit the measurements in a pseudo-linear portion of the complete polarization curve profile. The impedance expression is reported in the following *(6)*, [20]:

$$Z(w) = \frac{E_0 \sin(wt)}{I_0 \sin(wt + \varphi)} \quad (6)$$

where E_0 and I_0 represent respectively the sinusoidal amplitude of voltage and current, w is the angular frequency and φ is the phase angle.

These data were expressed through the impedance plot, Nyquist plot, where two resistances could be observed [20]:

- The first x-axis intercept, which represents the electrolyte/matrix ohmic resistance, an important parameter used to evaluate the matrix performance;
- The diameter of the semiarch, which is a measure of the polarization resistance.

3.1. Standard condition

Fig. 9 A presents the polarization curve in standard conditions, Table 3.

The obtained OCV is approximately 1.05 V, which is consistent with the Nernst eq. [21], exhibiting an error percentage in comparison with the results reported by Lan et al. [22]. The optimal operating point is around 0.8 V and 0.15 A/cm^{-2}, corresponding to a power density of

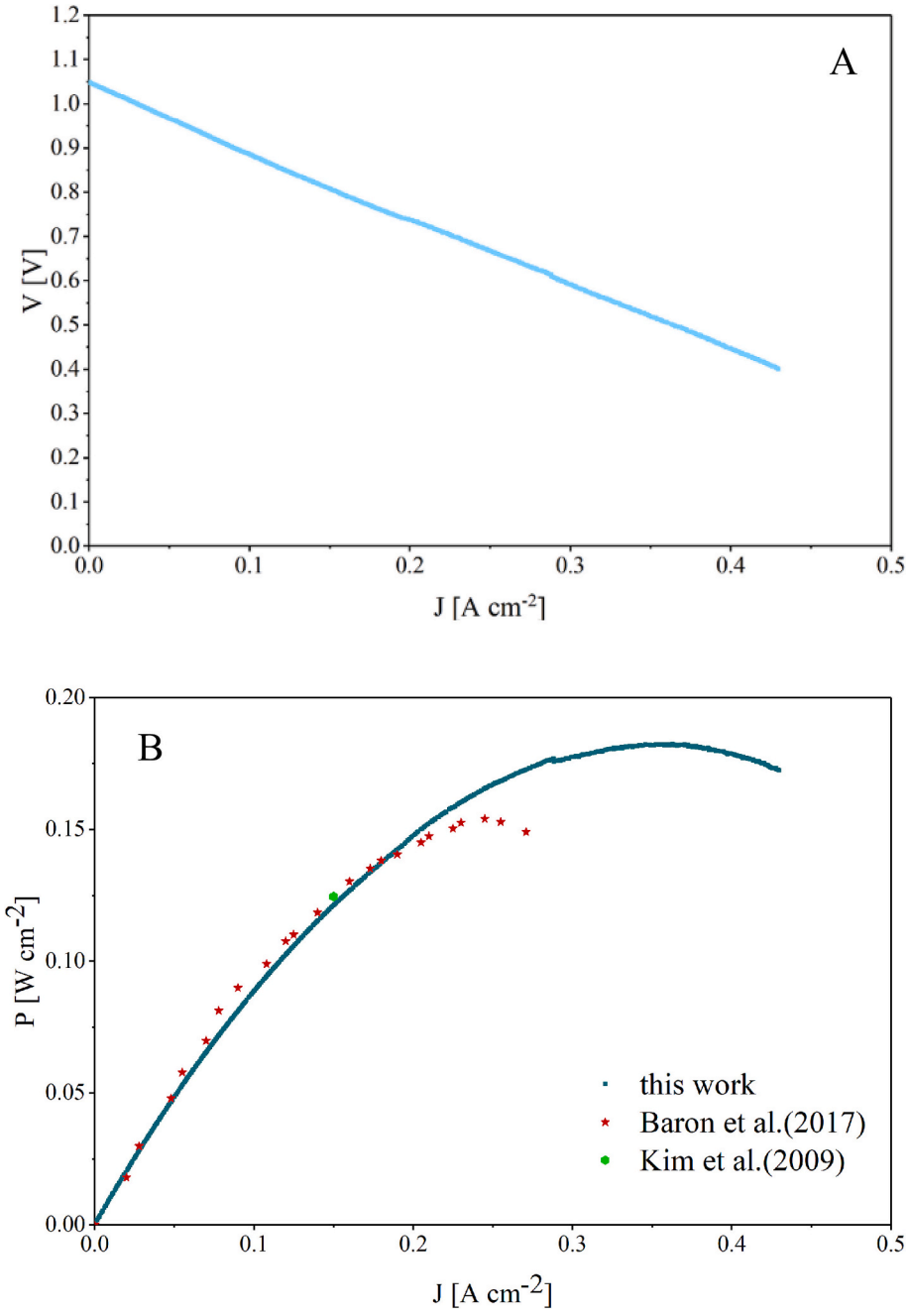

Fig. 9. A, Polarization curve @ standard conditions – 650 °C – Cathode $CO_2/O_2/H_2O/N_2$ 28.8/14.4/4/52.8 (vol%) – Anode $CO_2/H_2/H_2O$ 16.0/64.0/20.0 (vol%) – B, Power density curve and comparison between WUT and KIST results [16,17].

about 0.12 W·cm^{-2}. Choi et al. reported comparable performance under similar gas conditions, 0.125 W·cm^{-2} [23].

In addition, a comparison with the benchmark data from previous studies on matrix manufacturing proposed by WUT and KIST is reported in Fig. 9-*B*. It is particularly interesting to note that, in this work, despite operating under less favorable conditions due to the humidification of the inlet gas, the achieved performance is superior to that reported by Baron et al. Specifically, at a current density of 250 mA·cm^{-2}, our cell reaches a power density of 0.18 W·cm^{-2}, whereas Baron et al. reported 0.15 W·cm^{-2} under similar conditions (anode: H_2 80% – CO_2 20%; cathode: air 70% – CO_2 30%). This improvement is even more remarkable considering that the presence of water vapor in our feed gas typically reduces performance, while the higher hydrogen content in their setup should, in principle, have been more favorable for the electrochemical reaction. Kim et al. in their paper reported only the voltage versus time curve at an applied current density of 150 mA·cm^{-2}, and this value is consistent with the results presented in this work. Ćwieka et al. have investigated the substitution of the conventional nickel-based cathode, reporting power density values of up to 0.25 W·cm^{-2}, [24]; indicating that cell performance can be further enhanced through appropriate component selection.

As discussed earlier, EIS represents a crucial diagnostic tool. Fig. 10-*A* shows this measurement carried out with a sinusoidal perturbation of 5 mV over a frequency range from 20^4 to 10^{-1} Hz, generated by a galvanostat coupled to a frequency response analyzer (Zahner Zennium T5.9.2, Zahner-Elektrik GmbH & Co. KG, Kronach, Germany), recording ten points per decade of frequency. The internal resistance, corresponding to the ohmic resistance, is approximately 0.566 Ω·cm^2, in good

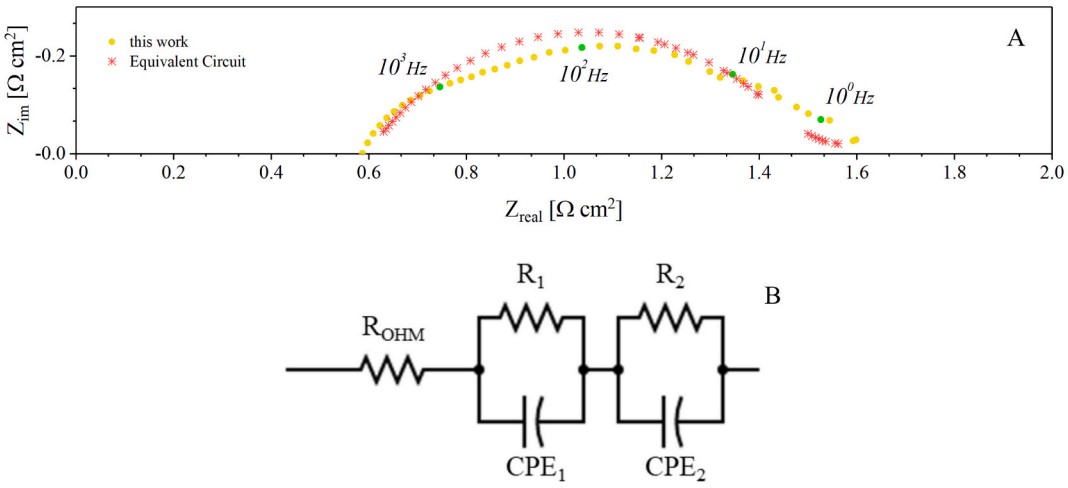

Fig. 10. A, EIS test performed in OCV @ standard condition – 650 °C – Cathode $CO_2/O_2/H_2O/N_2$ 28.8/14.4/4,0/52.8 (vol%) – Anode $CO_2/H_2/H_2O$ 16.0/64.0/20.0 (vol%) compared with the Equivalent Circuit fitting and B, Equivalent Circuit.

agreement with values reported in the literature [25]. Similarly, the polarization resistance, about 1.05 Ω·cm^2, is also consistent with literature [19,26].

In addition, the equivalent circuit (EC) proposed in Fig. 10-*B* was compared with the experimental data, showing good agreement between the EC model and the measured points, with a root mean square error (RMSE) of approximately 3. In this model, the ohmic resistance (R) is connected in series with two R//CPE (Constant Phase Element) circuits, which represent the anodic and cathodic contributions to the overall cell resistance. The use of CPEs accounts for the non-ideal capacitive behavior of the electrode–electrolyte interface, capturing surface heterogeneities and distributed time constants. This EC allows a quantitative interpretation of the impedance response and provides insight into the individual contributions of each electrochemical process within the cell.

Fig. 11 illustrates the temporal evolution of internal and polarization resistances. The data indicates that the cell undergoes a stabilization phase, during which the electrolyte progressively diffuses into the porous structure, filling the matrix and wetting the electrodes. Upon complete melting and subsequent diffusion of the salts, the resistances converge to a steady-state value [26]. Except for Fig. 11, all the data discussed were obtained after stabilizing at least 2 h.

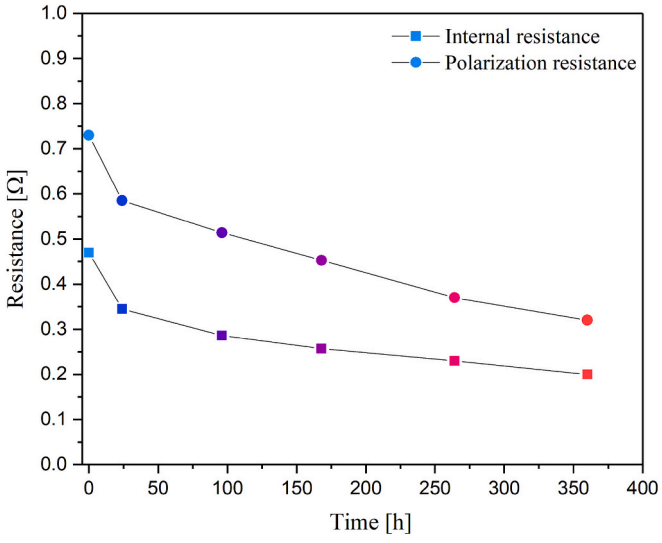

Fig. 11. Internal and Polarization Resistance variation with time @ standard condition – 650 °C – Cathode $CO_2/O_2/H_2O/N_2$ 28.8/14.4/4/52.8 (vol%) – Anode $CO_2/H_2/H_2O$ 16.0/64.0/20.0 (vol%). Total matrix thickness: 0.6 mm.

3.2. Temperature variation

Temperature plays a critical role in determining cell performance. As evidenced by the polarization curves obtained after cell stabilization in Fig. 12, higher operating temperatures lead to improved cell efficiency. However, this improvement is accompanied by a decrease in the OCV, which can be attributed to thermodynamic effects described by the Nernst equation, specifically, the reduction of Gibbs free energy with increasing temperature [26].

Fig. 13 presents the temperature dependence of the electrochemical impedance. The observed decrease in internal resistance (from 0.78 Ω cm^2 to 0.48 Ω cm^2) with increasing temperature is attributed to the improved ionic conductivity of the carbonate electrolyte. Moreover, as shown in *Fig. 13*, at lower temperatures the two impedance semicircles tend to merge into a single indicating that charge transfer and mass transport processes contribute simultaneously and cannot be clearly distinguished. This behavior is consistent with literature reports, which attribute the performance degradation at lower temperatures to the increased resistance associated with these processes [27].

The ohmic resistance, is typically described by an exponential function as reported in Eq. (7), [28],

$$R_\Omega = P_1 e^{P_2/T} \tag{7}$$

Experimental data at different temperatures were used to fit the curve shown in Fig. 14 and in Table 4 the kinetic parameters to define the ohmic resistance were reported. Fig. 14 also reports the results of Bosio et al. Both datasets follow the expected exponential trend; however, it is evident that those literature cells exhibit lower internal resistance. This difference can be attributed to the matrix thickness and electrolyte diffusion properties.

3.3. Cathode gas composition variation

Additional tests were performed under varying cathode flow conditions, as shown in Table 5.

As expected, Fig. 15, the reduction of CO_2 leads to a decrease in cell performance. However, an intriguing observation is that, while the IV curves were expected to exhibit a diverging trend at higher currents, a second curvature appears at elevated current densities. This suggests the presence of an additional ionic carrier, likely hydroxide ions (OH^-)

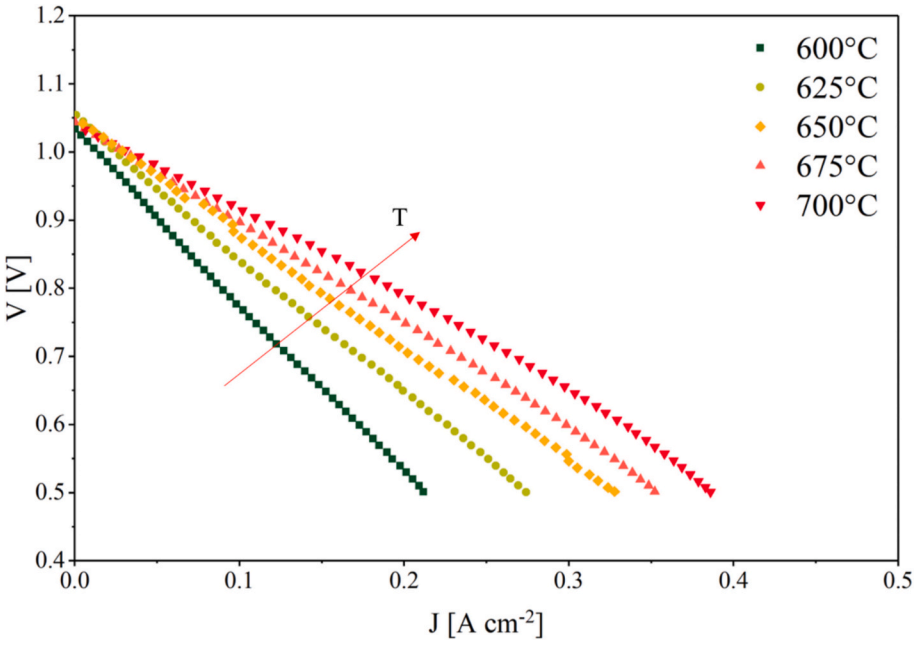

Fig. 12. Polarization curve - Temperature variation @ standard condition – Cathode $CO_2/O_2/H_2O/N_2$ 28.8/14.4/4/52.8 (vol%) – Anode $CO_2/H_2/H_2O$ 16.0/64.0/20.0 (vol%).

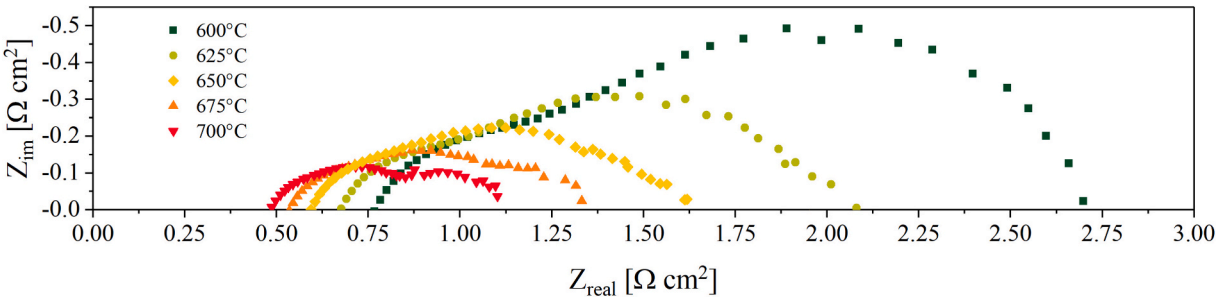

Fig. 13. EIS curve - Temperature variation @ standard condition – Cathode $CO_2/O_2/H_2O/N_2$ 28.8/14.4/4/52.8 (vol%) – Anode $CO_2/H_2/H_2O$ 16.0/64.0/20.0 (vol%).

[28–30].

From the Fig. 15, it can be observed that the performance of the MCFC decreases primarily when the amount of CO_2 is reduced, as expected from theoretical considerations, for both Series A and Series B. Additionally, the CO_2/O_2 ratio, as previously highlighted in other studies [31], also affects cell performance. Specifically, when the ratio is lower than 1/3 (cases A-1 and B-1), variations in oxygen concentration do not lead to significant changes in performance, even at high current densities. However, when the ratio increases (as shown in the other pairs A-2 and B-2, A-3 and B-3, A-4 and B-4), the configurations with a higher CO_2/O_2 ratio (Test Series A) exhibit a performance penalty compared to the corresponding cases with a lower ratio (Test Series B), especially at higher current densities. At lower current densities, this effect becomes negligible, as also reported in previous literature [31].

Additionally, the power densities for Test Series A and Test Series B are reported in Fig. 16. As expected, increasing the CO_2 content in both test series leads to a rise in power density. In particular, when the O_2 concentration increases from 15% to 30%, a higher number of electrochemical reactions occur, resulting in an increase in the measured power density.

3.4. Real application conditions

Up to this point, all operating conditions have been tailored ad hoc to assess the functionality of the materials and the cell itself. This implies that most tests were conducted with a high concentration of CO_2, which enhances ion transport and, consequently, electron flow. However, it is also of great interest to investigate performance under real-world conditions, particularly those relevant to CCS applications. Among the sectors most affected by carbon emissions are the maritime and metallurgical industries [32,33].

Based on these considerations, additional tests were carried out to evaluate the cell's performance under realistic operating conditions. In particular, Risso et al. and Yoni et al. [34,35]. proposed representative scenarios for the maritime and metallurgical sectors, respectively. It is important to highlight that the flue gases emitted by ships are directly suitable for use in this type of cell. In contrast, although CO_2 concentrations in metallurgical emissions are higher, the oxygen content is insufficient to sustain the electrochemical reaction, (2). As a result, supplemental oxygen must be added, which in turn reduces the percentage of CO_2 available.

The main consequence of operating with a lower CO_2 concentration is that CO_2 becomes the limiting reactant, leading to a reduction in overall cell performance compared to the standard condition. Fig. 17 presents the polarization and power density curves for both application scenarios.

Analysis of the graph reveals that the power density reaches approximately 70 mW/cm^2, a value that is fully consistent with those

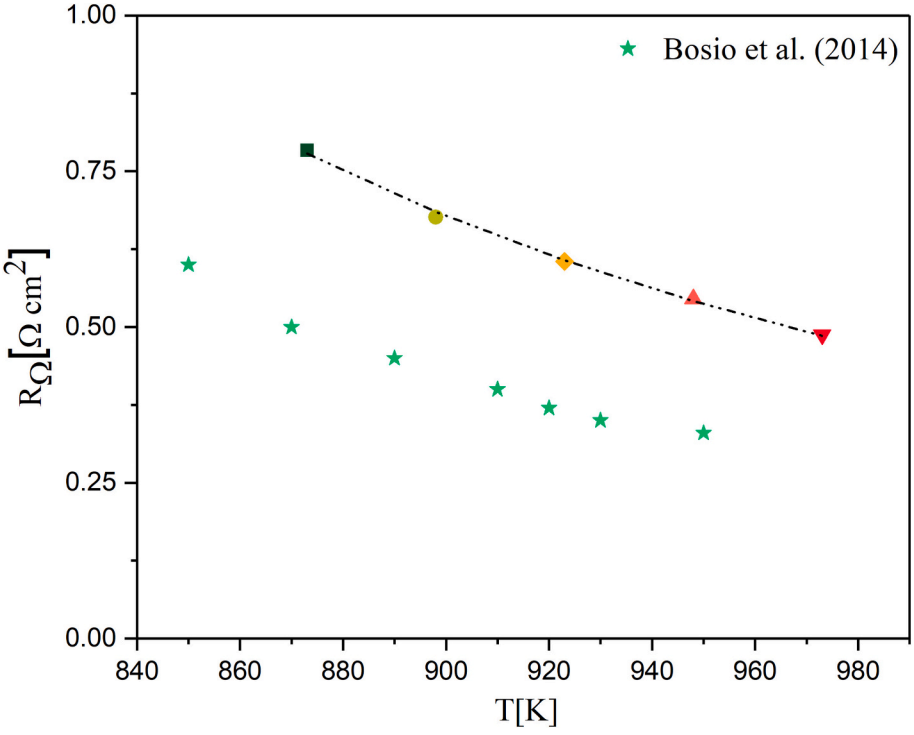

Fig. 14. Experimental function of the internal resistance @ different temperatures (600 °C – 625 °C – 650 °C – 675 °C – 700 °C) and comparison with the literature result, [28].

Table 4
Ohmic resistance kinetic parameters.

P_1 $[\Omega^* cm^2]$	$P_2[K]$	Reference
0.0079 ± 0.00098	3999 ± 111.9	This study
0.0139	3054	[29]

Table 5
Experimental campaigns: A and B respectively 15% and 30% of O_2 with CO_2 variation 5–20% [step 5%].

–		–	Anode	Cathode
			$CO_2/H_2/H_2O$	$CO_2/O_2/H_2O/N_2$
A	$CO_{2,\ Cathode}$, effect, [vol%]	1	16.0/64.0/20.0	5.0/15.0/4.0/76.0
		2		10.0/15.0/4.0/71.0
		3		15.0/15.0/4.0/66.0
		4		20.0/15.0/4.0/61.0
B	$CO_{2,\ Cathode}$, effect, [vol%]	1	16.0/64.0/20.0	5.0/30.0/4.0/61.0
		2		10.0/30.0/4.0/56.0
		3		15.0/30.0/4.0/51.0
		4		20.0/30.0/4.0/46.0

reported in other studies on CCS [36]. The integration of MCFCs into CCS systems represents an innovative approach, combining high CO_2 selectivity with efficient power generation. Unlike conventional CCS technologies, which require a continuous energy input for CO_2 capture, MCFCs demand energy only during the start-up phase to reach the operating temperature, while subsequently producing electricity during operation [37].

4. Conclusions

The objective of this study was to analyze the manufacturing process of the matrix, a critical component of Molten Carbonate Fuel Cells (MCFCs), through a series of analyses aimed at characterizing and evaluating its properties. The main innovation of this study is the replacement of toluene with an environmentally friendly organic solvent provided by Ecospray Technology, density at 20 °C 790 kg/m^3, molecular weight 53 g/mol, viscosity at 25 °C 0.5 mPa·s, and boiling point 65 °C).

Two primary characterization techniques were employed: SEM and mercury porosimetry. SEM analysis revealed a homogeneous surface morphology, while mercury porosimetry provided key quantitative parameters, namely, a porosity of 62%, a specific surface area of 15 m^2/g and 50% of the pores with diameters smaller than 0.167 μm.

Electrochemical testing suggests the high performance of the developed matrix, measuring an open-circuit voltage of 1.05 V and a peak power density of approximately 120 mW/cm^2 at a current density of 1500 A/m^2. Electrochemical Impedance Spectroscopy indicated a low internal resistance of 0.566 Ω·cm^2 at 650 °C, in good agreement with values reported in the literature. Moreover, the matrix showed encouraging results under simulated conditions relevant to hard-to-abate applications, such as maritime transport and the steel industry, achieving a power density of approximately 70 mW/cm^2.

Overall, the newly developed formulation represents a significant step forward in MCFC technology, as it enables a more sustainable, safer, and potentially more scalable manufacturing process. The adoption of a green solvent with suitable physical properties may facilitate large-scale matrix production by reducing environmental impact, improving process safety, and easing compliance with industrial regulations. From a broader perspective, this fabrication route supports the industrial deployment of MCFC systems, contributing to their viability as a key technology for decarbonization in energy-intensive sectors.

CRediT authorship contribution statement

Lucia Cardona: Writing – review & editing, Writing – original draft, Visualization, Methodology, Investigation, Conceptualization. **Riccardo Risso:** Writing – review & editing, Conceptualization. **Juan Pedro Pérez Trujillo:** Writing – review & editing, Supervision,

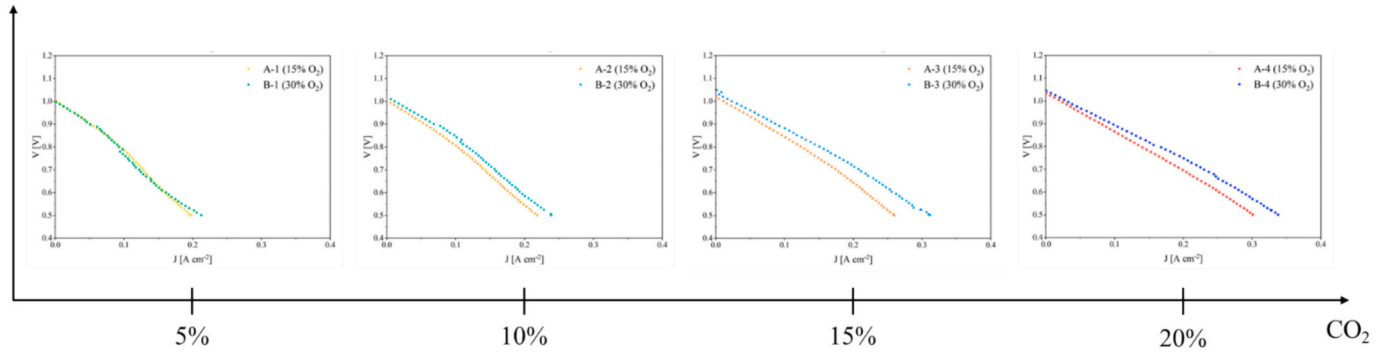

Fig. 15. Polarization curves obtained by varying the CO_2 content (1–5%, 2–10%, 3–15%, 4–20%) and the O_2 content (A – 15%, B – 30%). At lower CO_2 concentrations, carbon dioxide becomes the limiting factor for the electrochemical reaction. As the CO_2 and O_2 contents increase, the performance of the cell improves, and the difference between the curves becomes more evident.

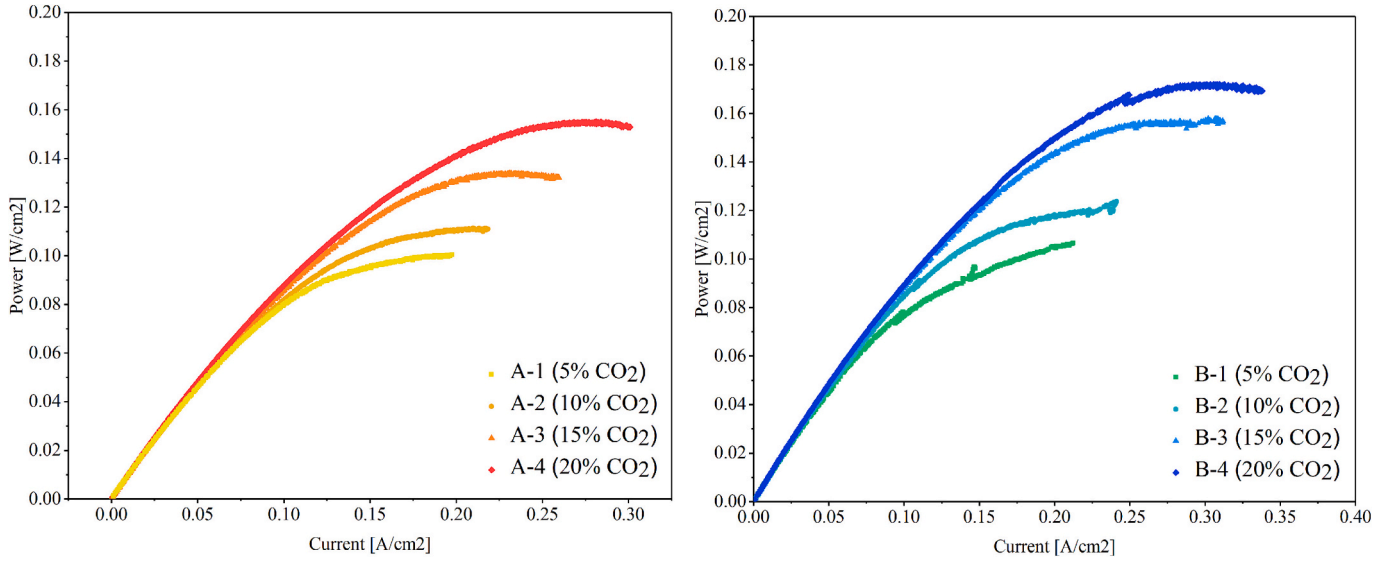

Fig. 16. Power Density Test Series A (15% O_2) and Test Series B (30% O_2), by varying the amount of CO_2 (5%-10%-15%-20%).

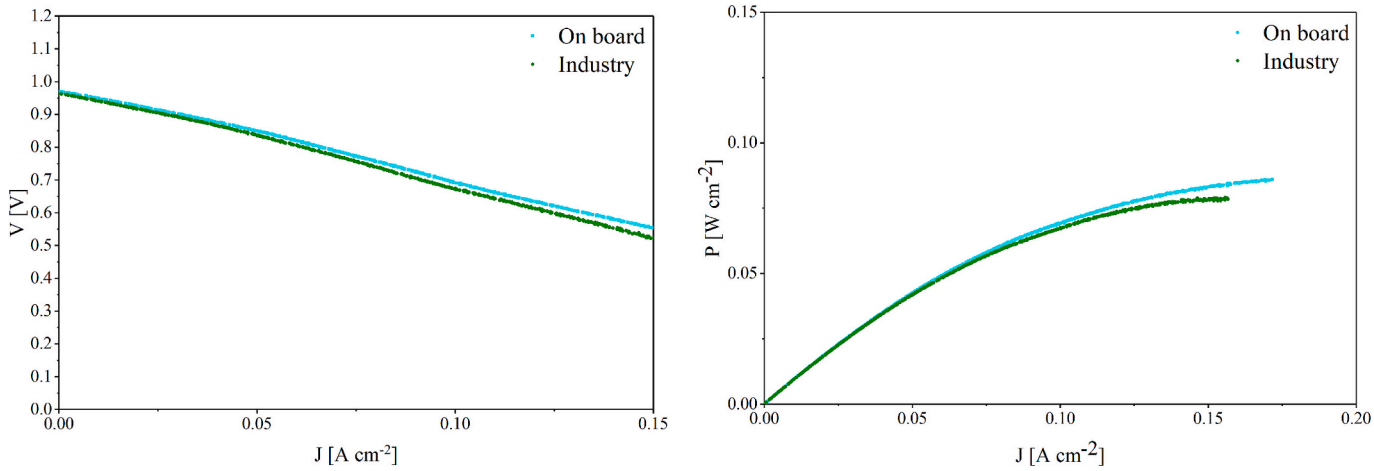

Fig. 17. Polarization and Power density curves in maritime and metallurgical industries.

Conceptualization. **Dario Bove:** Writing – review & editing, Supervision, Conceptualization. **Carina Lagergren:** Supervision, Project administration. **Maurizio Archetti:** Supervision, Project administration. **Barbara Bosio:** Writing – review & editing, Supervision, Project administration, Conceptualization.

Declaration of competing interest

The authors declare that they have no known competing financial interests or personal relationships that could have appeared to influence the work reported in this paper.

Acknowledgements

This research was partially funded by the project CALIPSO – Celle a combustibile innovative ad alta potenza in sistemi stazionari e di mobilità. PNRR – Prog. n. RSH2A_000021 - CUP: F57G25000200006.

The authors gratefully acknowledge Dott. Paola Stagnaro and Dott. Roberto Utzeri of CNR-SCITEC for the collaboration in the partial characterization of the components.

Data availability

The data that has been used is confidential.

References

[1] Sustainable Development Goals, (n.d.). https://unric.org/en/united-nations-sustainable-development-goals/ (accessed January 18, 2026).
[2] B. Bosio, M. Archetti, E. Audasso, D. Bove, Process analysis of a molten carbonate fuel cell on-board application to reduce vessel CO2 emissions, Chem. Eng. Process. - Process Intensif. 190 (2023), https://doi.org/10.1016/j.cep.2023.109415.
[3] M. Archetti, E. Audasso, B. Bosio, D. Bove, High temperature fuel cells to reduce CO2 emission in the maritime sector, E3S Web Conf. 334 (2022), https://doi.org/10.1051/e3sconf/202233404013.
[4] D. Marra, B. Bosio, Process analysis of 1 MW MCFC plant, Int. J. Hydrogen Energy 32 (2007) 809–818, https://doi.org/10.1016/j.ijhydene.2006.11.016.
[5] U.S. Department of Energy, Fuel Cell Handbook, 7th ed, National Energy Technology Laboratory, 2004.
[6] J. Milewski, T. Wejrzanowski, K. Fung, K. Cwieka, K. Li, Supporting ionic conductivity of Li 2 CO 3 / K 2 CO 3 molten carbonate electrolyte by using yttria stabilized zirconia matrix, Int. J. Hydrogen Energy 6 (2021).
[7] Milewski, J., Dybiński, O., Szczęśniak, A., Martsinchyk, A., Ćwieka, K., Xing, W., & Szabłowski, Ł. (2024). Identification of oxygen ion conductivity of Ba doped Bi0.5Na0.5TiO3 (Ba-BNT) based matrix impregnated by lithium/potassium electrolyte for molten carbonate fuel cells. Int. J. Hydrogen Energy, 51(Part D), 412–423. doi:https://doi.org/10.1016/j.ijhydene.2023.06.116.
[8] J.A. Lewis, Colloidal processing of ceramics, J. Am. Ceram. Soc. 83 (2000) 2341–2359, https://doi.org/10.1111/j.1151-2916.2000.tb01560.x.
[9] M.N. Rahaman, Ceramic processing and sintering. 2nd ed., CRC press, boca Raton, FL, USA, doi:https://doi.org/10.1201/9781315274126.
[10] G.W. Scherer, Theory of drying, J. Am. Ceram. Soc. 73 (1990) 3–14, https://doi.org/10.1111/j.1151-2916.1990.tb05082.x.
[11] R. E. Mistler, E. R. Twiname, Tape casting: theory and practice, Wiley–American ceramic society, Westerville, OH, USA, ISBN: 978-1-574-98029-5.
[12] C. J. Brinker, G. W. Scherer, Sol–gel science: the physics and chemistry of sol–gel processing, Academic press, Boston, MA, USA, ISBN: 978-0-12-134970-7.
[13] A.A. Sheikh, F.R. Bianchi, D. Bove, B. Bosio, et al., Matrix structure, key features, and degradation issues in molten carbonate fuel cells: state-of-the-art review with emphasis on lithium aluminate $LiAlO_2$ and reinforcements, Heliyon 10 (2024) e25847, https://doi.org/10.1016/j.heliyon.2024.e25847.
[14] S.K. Rajput, S. Singh, R. Bhardwaj, Toluene Toxicity: Outline, Management, and Prognosis, Elsevier Inc., 2024, https://doi.org/10.1016/B978-0-323-95235-4.00052-9.
[15] C. Capello, S. Hellweg, K. Hungerbühler, Environmental assessment of waste-solvent treatment options: part II: general rules of thumb and specific recommendations, J. Ind. Ecol. 12 (2008) 111–127, https://doi.org/10.1111/j.1530-9290.2008.00009.x.
[16] J.E. Kim, J. Han, S.P. Yoon, S.W. Nam, T.H. Lim, H. Kim, Mechanical properties of the lithium aluminate matrix for MCFC reinforced with metal oxide materials, Curr. Appl. Phys. 10 (2010) 73–76, https://doi.org/10.1016/j.cap.2009.11.046.
[17] R. Baron, T. Wejrzanowski, J. Milewski, Ł. Szabłowski, A. Szczęśniak, K.Z. Fung, Manufacturing of Γ-LiAlO2 matrix for molten carbonate fuel cell by high-energy milling, Int. J. Hydrogen Energy 43 (2018) 6696–6700, https://doi.org/10.1016/j.ijhydene.2018.02.085.
[18] Anton Paar, PoreMaster, (n.d.). https://www.anton-paar.com/it-it/prodotti/dettagli/serie-poremasterr/?prd=31038 (accessed January 18, 2026).
[19] J.P. Perez Trujillo, G. Lindbergh, C. Lagergren, Unravelling electrolyte dynamics in reversible molten carbonate fuel cells through distribution of relaxation times, Int. J. Hydrogen Energy. draft (2024) 1342–1354. doi:https://doi.org/10.1016/j.ijhydene.2024.10.124.
[20] A.C. Lazanas, M.I. Prodromidis, Electrochemical impedance Spectroscopy—A tutorial, ACS Meas. Sci. Au. 3 (2023) 162–193, https://doi.org/10.1021/acsmeasuresciau.2c00070.
[21] W. Virginia, Fuel cell handbook 26 (1989), 26-6292-26–6292.
[22] L. Hu, G. Lindbergh, C. Lagergren, Performance and durability of the molten carbonate electrolysis cell and the reversible molten carbonate fuel cell, J. Phys. Chem. C 120 (2016) 13427–13433, https://doi.org/10.1021/acs.jpcc.6b04417.
[23] H.J. Choi, J.J. Lee, S.H. Hyun, H.C. Lim, Fabrication and performance evaluation of electrolyte-combined α-LiAlO2 matrices for molten carbonate fuel cells, Int. J. Hydrogen Energy 36 (2011) 11048–11055, https://doi.org/10.1016/j.ijhydene.2011.05.184.
[24] K. Ćwieka, A. Lysik, T. Wejrzanowski, T. Norby, W. Xing, Microstructure and electrochemical behavior of layered cathodes for molten carbonate fuel cell, 500 (2021).
[25] S. Lo Conte, S. Mataloni, M. Della Pietra, L. Simonetti, Y. De Pra, M.C. Annesini, DRT-based electrochemical investigation on the fuel electrode in a molten carbonate electrolysis cell, J. Power Sources 631 (2025), https://doi.org/10.1016/j.jpowsour.2025.236197.
[26] C.O. Colpan, Y. Nalbant, M. Ercelik, Fundamentals of fuel cell technologies, Elsevier, 2018, https://doi.org/10.1016/B978-0-12-809597-3.00446-6.
[27] S. Koomson, S.H. Bae, K.M. Kim, C.G. Lee, Effect of temperature on the electrode overpotential of molten carbonate electrolysis and fuel cells with inert-gas step addition method, J. Electroanal. Chem. 950 (2023) 117844, https://doi.org/10.1016/j.jelechem.2023.117844.
[28] T.A. Barckholtz, H. Elsen, P.H. Kalamaras, G. Kiss, J. Rosen, D. Bove, E. Audasso, B. Bosio, Experimental and modeling investigation of CO3=/OH– equilibrium effects on molten carbonate fuel cell performance in carbon capture applications, Front. Energy Res. 9 (2021) 1–15, https://doi.org/10.3389/fenrg.2021.669761.
[29] B. Bosio, N. Di Giulio, S.W. Nam, A. Moreno, An effective semi-empiric model for MCFC kinetics: theoretical development and experimental parameters identification, Int. J. Hydrogen Energy 39 (2014) 12273–12284, https://doi.org/10.1016/j.ijhydene.2014.04.119.
[30] E. Audasso, B. Bosio, D. Bove, E. Arato, T. Barckholtz, G. Kiss, J. Rosen, H. Elsen, R. B. Gutierrez, L. Han, T. Geary, C. Willman, A. Hilmi, C.Y. Yuh, H. Ghezel-Ayagh, New, dual-anion mechanism for molten carbonate fuel cells working as carbon capture devices, J. Electrochem. Soc. 167 (2020) 084504, https://doi.org/10.1149/1945-7111/ab8979.
[31] E. Audasso, B. Bosio, S. Nam, Extension of an effective MCFC kinetic model to a wider range of operating conditions, Int. J. Hydrogen Energy 41 (2016) 5571–5581, https://doi.org/10.1016/j.ijhydene.2015.10.152.
[32] W. Chung, K. Roh, J.H. Lee, Design and evaluation of CO2 capture plants for the steelmaking industry by means of amine scrubbing and membrane separation, Int. J. Greenhouse Gas Control 74 (2018) 259–270, https://doi.org/10.1016/j.ijggc.2018.05.009.
[33] R. Risso, L. Cardona, M. Archetti, F. Lossani, B. Bosio, D. Bove, A review of on-board carbon capture and storage techniques: solutions to the 2030 IMO regulations, Energies 16 (2023) 1–26, https://doi.org/10.3390/en16186748.
[34] R. Risso, D. Bove, B. Bosio, Comparative analysis of different on-board CCS molten carbonate fuel cell solutions for IMO compliance, Greenh. Gases Sci. Technol. (2025), https://doi.org/10.1002/ghg.70011.
[35] Y. Austen, D. Bove, F. Cannizzaro, E. Palmisani, B. Bosio, Exploring the potential of molten carbonate fuel cells for CO2 capture and concentration: a feasibility analysis in the steel industry, Energy Fuel 39 (50) (2025) 23703–23714, https://doi.org/10.1021/acs.energyfuels.5c04152.
[36] A. De Silvestri, S. Stendardo, M. Della Pietra, D. Borello, Decarbonizing cement plants via a fully integrated calcium looping-molten carbonate fuel cell process: assessment of a model for fuel cell performance predictions under different operating conditions, Int. J. Hydrogen Energy 46 (2021) 14988–15007, https://doi.org/10.1016/j.ijhydene.2020.12.024.
[37] S. Ferguson, A. Tarrant, Molten carbonate fuel cells for 90% post combustion CO2 capture from a new build CCGT, Front. Energy Res. 9 (2021) 1–6, https://doi.org/10.3389/fenrg.2021.668431.